

**Search for High Mass Neutral Bosons Decaying to Tau
Pairs with the CMS Experiment**

by

A. A. Johnson

B.S., Carnegie Mellon University, 2011

M.S., University of Colorado, 2013

A thesis submitted to the
Faculty of the Graduate School of the
University of Colorado in partial fulfillment
of the requirements for the degree of
Doctor of Philosophy
Department of Physics
2016

This thesis entitled:
Search for High Mass Neutral Bosons Decaying to Tau Pairs with the CMS Experiment
written by A. A. Johnson
has been approved for the Department of Physics

Prof. John P. Cumalat

Prof. Kevin Stenson

Prof. Steven Wagner

Date _____

The final copy of this thesis has been examined by the signatories, and we find that both the content and the form meet acceptable presentation standards of scholarly work in the above mentioned discipline.

Johnson, A. A. (Ph.D., Physics)

Search for High Mass Neutral Bosons Decaying to Tau Pairs with the CMS Experiment

Thesis directed by Prof. John P. Cumalat

Two searches for heavy neutral resonances, Z' 's, decaying to back-to-back tau pairs are carried out using the Compact Muon Solenoid experiment at the Large Hadron Collider. The first, carried out during the 2012 data-taking run at $\sqrt{s} = 8$ TeV, focuses on the fully-leptonic channel, in which one tau decays to an electron and the other to a muon. The second, carried out during the 2015 run at $\sqrt{s} = 13$ TeV, focuses on the fully-hadronic channel, in which each tau decays to a hadronic jet. Each search employs a hybrid of background estimation strategies using both Monte Carlo simulation and data-driven methods. In both searches, observed data is found to be in agreement with Standard Model expectation and no excesses are observed. Limits are placed on the Z' , culminating in a world-record limit of 2.2 TeV at 95% confidence level.

Dedication

To my parents, Carl and Sharon Johnson. Without your constant love, support, and encouragement, none of this would have been remotely possible.

Acknowledgements

Here's where you acknowledge folks who helped. But keep it short, i.e., no more than one page, as required by the Grad School Specifications.

Contents

Chapter

1	Outline	1
1.1	Standard model	1
1.2	The CMS Experiment	1
1.3	EMu channel @ 8TeV	2
1.4	TauTau channel @ 13TeV	2
2	Introduction	3
2.1	Introduction	3
3	The Standard Model	5
3.1	Particles of the Standard Model	5
3.2	Quantum Electrodynamics	7
3.3	Electroweak Theory	9
3.4	Quantum Chromodynamics	11
3.5	Spontaneous Symmetry Breaking and the Higgs Mechanism	12
4	Beyond the Standard Model	15
5	The Compact Muon Solenoid (CMS) Experiment	17
5.1	The silicon tracker	18
5.1.1	The pixel detector	19

5.1.2	The strip tracker	21
5.2	The electromagnetic calorimeter	21
5.3	The hadronic calorimeter	22
5.4	The CMS magnet	23
5.5	The muon system	24
5.5.1	Drift tubes (DTs)	25
5.5.2	Cathode strip chambers (CSCs)	25
5.5.3	Resistive plate chambers (RPCs)	26
5.6	The trigger system	26
5.6.1	The Level-1 (L1) trigger)	27
5.6.2	The High level trigger (HLT)	27
5.7	Particle Reconstruction	28
5.7.1	Particle Flow	28
6	Results	34
6.1	13 TeV Results	34
6.2	8 TeV Results	36

Appendix

Tables

Table

6.1	Number of observed events in data and estimated background events for the whole mass range. The uncertainties quoted on the number of background events represent the combined statistical and systematic uncertainty.	34
6.2	Number of observed events in data and estimated background events in the region $M(\tau_1, \tau_2, \cancel{E}_T) > 300$ GeV. The uncertainties quoted on the number of background events represent the combined statistical and systematic uncertainty.	35
6.3	Event summary table after signal region selection	36

Figures

Figure

3.1	Table showing the quarks, leptons, and gauge bosons (force carriers) in the SM as well as the Higgs boson	6
3.2	Typical QED interaction	9
4.1	$Z' \rightarrow \tau\tau$ event at the LHC, wherein two quarks from colliding protons form a Z' which then decays to an oppositely-charged, back-to-back pair of τ leptons.	16
5.1	The Large Hadron Collider located underneath the Franco-Swiss border at CERN near Geneva, Switzerland. The CMS Experiment is located on the French side in Cessy, France	17
5.2	The CMS Experiment (open for maintenance)	18
5.3	Schematic of the CMS Experiment showing the silicon trackers, electromagnetic calorimeter (ECAL), hadronic calorimeter (HCAL), superconducting solenoid, steel return yoke, and muon system.	19
5.4	Overview of the silicon tracker layout.	20
5.5	Diagram indicating the layout of the barrel pixel (BPIX) sensors (in green) and endcap pixel (FPIX) sensors (in pink)	20
5.6	Layout of the electromagnetic calorimeter (ECAL) indicating the configuration of the barrel (EB) and endcap (EE) crystals.	22

5.7	Layout of the hadronic calorimeter (HCAL) indicating the configuration of the barrel (HB) and endcap (HE) components as well as the outer HCAL (HO) lining the solenoid.	23
5.8	The superconducting solenoid.	24
5.9	Layout of the muon system highlighting the layered structure of the drift tubes (DTs, green), cathode strip chambers (CSCs, blue), and resistive plate chambers (RPCs, red).	25
6.1	Top Left: $m(\mu, \tau_h, \cancel{E}_T)$ distribution in the signal region, in log scale. Top Right: $m(\tau_h, \tau_h, \cancel{E}_T)$ distribution in the signal region, in log scale. Bottom Left: $m(e, \tau_h, \cancel{E}_T)$ distribution in the signal region, in log scale. Bottom Right: $m(e, \mu, \cancel{E}_T)$ distribution in the signal region, in log scale.	37
6.2	Expected and observed limits for the $\tau_\mu\tau_h$, $\tau_h\tau_h$, $\tau_e\tau_h$, $\tau_e\tau_\mu$ channels. A k factor of 1.3 has been used to scale the leading order (LO) signal cross-section.	38
6.3	Combined expected limit for the $\tau_\mu\tau_h$, $\tau_h\tau_h$, $\tau_e\tau_h$, $\tau_e\tau_\mu$ channels.	39
6.4	Combined expected limit for the $\tau_\mu\tau_h$, $\tau_h\tau_h$, $\tau_e\tau_h$, $\tau_e\tau_\mu$ channels. A k factor of 1.3 has been used to scale the leading order (LO) signal cross-section.	39
6.5	$m(e, \tau_h, \cancel{E}_T)$ distribution for SR in 8TeV search. A 1.5TeV Z'_{SSM} sample is also included.	39
6.6	Expected background rates compared to observed rates in bins of $m(e, \tau_h, \cancel{E}_T)$. Uncertainties are statistical in each bin.	40
6.7	Expected signal rates and associated significances in bins of $m(e, \tau_h, \cancel{E}_T)$.	40
6.8	95% CL upper limit on $\sigma(pp \rightarrow Z')(Z' \rightarrow \tau\tau)$ as a function of Z' mass. The color bands on the expected limits represent one standard deviation (green) and two standard deviations (yellow).	40

Chapter 1

Outline

OUTLINE

1.1 Standard model

Z'

Why TauTau

Other BSM theories involving ditau pairs

1.2 The CMS Experiment

Pixels

Monitoring tool

Strips

ECAL

HCAL

Muon System

Triggering

L1 HLT

Computing @ CERN

1.3 EMu channel @ 8TeV

MC samples used
Generation methods
Data samples used
Object selection
Validation
Background estimation
Lifetime cuts optimization
Systematics
Limit setting methodology impact of lifetime cuts on limit

1.4 TauTau channel @ 13TeV

MC samples used
Generation methods
Data samples used
Object selection
Validation
Background estimation
Lifetime cuts optimization
Systematics
Limit setting methodology impact of lifetime cuts on limit

Chapter 2

Introduction

2.1 Introduction

The mission of particle physics is to increase our understanding of the most fundamental constituents of our universe and their interactions. These efforts have arguably been going on since the era of the Greek philosophers, who classified all matter into the elemental categories of earth, air, wind, and fire. As the centuries progressed, our knowledge of the nature of the universe has been refined as new theories were proposed to explain the phenomena we observe in nature, and, at the same time, more and more sophisticated experiments were designed to test them. Particle physics as a field today is broadly divided into two sub-fields: theory and experiment. Theorists seek to develop models that offer a more complete explanation of particle interactions, and experimentalists are tasked with validating these models. Efforts in particle theory in the late-20th century culminated in the Standard Model (SM) of particle physics, which has proven to be tremendously successful at describing a large number of observed particle phenomena (some which have been accurately validated to one part in ten billion!).

The SM is not without its deficiencies, however. Today, there remain many open questions in particle physics that are not sufficiently (or at all) addressed by the SM. To name just a few:

Why is there more matter than antimatter in the universe? What is dark matter? What is dark energy? Can the strong interaction be unified with the electroweak interaction? Why is the Higgs mass 125 GeV and not at the Planck scale?

Attempts to answer these questions require new theories modifying and building on the SM.

These theories must then be tested, which is where the experimentalists come in. While the SM was perhaps the crowning achievement of high energy theory in the twentieth century, the Large Hadron Collider (LHC) is arguably the most noteworthy undertaking in high energy experiment in the twenty-first. Located in Geneva, Switzerland at the European Organization for Nuclear Research (CERN, from the French “Conseil Européen pour la Recherche Nucléaire”), the LHC is the highest-energy particle collider ever built and has been an invaluable tool in the quest to validate theories of new physics.

This thesis presents an effort to use one of the primary experiments on the LHC, the Compact Muon Solenoid (CMS), to search for a new particle, called the Z' , predicted by many such “Beyond Standard Model” (BSM) theories. Part I will lay the groundwork, offering an overview of the SM and the modifying theories which predict the Z' ’s existence. Part II will discuss the tools used in the search: the LHC, the CMS experiment, and the substantial computing resources needed to conduct a full search for new physics. Part III will discuss the search during the 2012 data-taking run at the LHC, and Part IV will discuss the most recent search conducted during the 2015 run. Part V will offer an overview of future possibilities in this search effort as well as concluding remarks.

Part I

Chapter 3

The Standard Model

As mentioned, the Standard Model (SM) of particle physics is the set of theories describing subatomic particles and their interactions according to the electromagnetic, weak, and strong forces. Describing these interactions individually are the theory of quantum electrodynamics (QED, electromagnetic), electroweak theory (EW, weak and electromagnetic), and the theory of quantum chromodynamics (QCD, strong). These individual theories combine to form the symmetry group describing the SM:

$$SU(3)_C \times SU(2)_L \times U(1)_Y$$

where $SU(3)_C$ is the symmetry group describing QCD, while $SU(2)_L \times U(1)_Y$ together are the symmetry groups describing electroweak theory, the unification of the electromagnetic and weak interactions.

This chapter will begin with an overview of the fundamental particles in the SM, and then will provide a brief discussion of each of the constituent theories listed above. It will conclude with additional sections on specific elements of the SM which are especially relevant to searches for new physics at hadron colliders.

3.1 Particles of the Standard Model

Shown in Figure 3.1, the particles included in the SM are believed to be fundamental (that is, they cannot be broken down into smaller constituent particles). Broadly, these particles can be

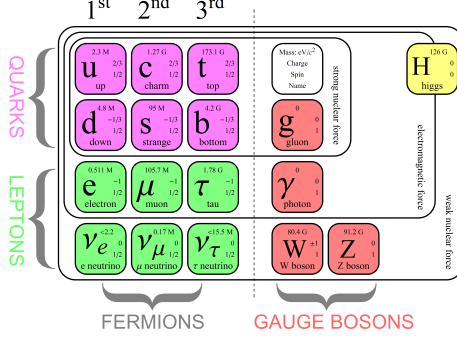


Figure 3.1: Table showing the quarks, leptons, and gauge bosons (force carriers) in the SM as well as the Higgs boson

divided into spin-1/2 particles, known as fermions, and integer-spin particles, known as bosons.

Fermions make up the matter of our universe. They are further divided into quarks and leptons. Quarks combine with other quarks to form *hadrons*: baryons such as protons and neutrons forming atomic nuclei, and with other antiquarks to form mesons such as pions and kaons. Quarks have electric charge and interact via the electromagnetic and weak forces, and they also have color charge, meaning they interact via the strong force as well. This strong force is what keeps baryons and mesons held together and will be discussed further in the section on QCD. Quarks are divided into pairs of positive and negative charge across three “generations” of increasing mass. In each pair, the positively-charged quark has electric charge $+2/3$ and the negatively-charged quark has electric charge $-1/3$. The first generation consists of the positively-charged *up* (*u*) quark and the negatively-charged *down* (*d*) quark. These are the quarks most commonly found in matter as they make up protons and neutrons in matter as well as the majority of pions. The second generation consists of the positively-charged *charm* (*c*) quark and the negatively-charged *strange* (*s*) quark. These quarks form more exotic hadrons such as kaons and lambdas. The third generation consists of the positively-charged *top* (*t*) quark and the negatively-charged *bottom* (*b*) quark. These are quite heavy, quite short-lived quarks which are rarely found in bound states.

While the quarks interact via both the strong and electroweak forces, the leptons only experience the electroweak interaction. The nature of this interaction will be discussed further in the sections on QED and EW theory. Like the quarks, the leptons are divided into three generations.

Each generation consists of a negatively-charged particle with charge -1, and a companion neutrino which is electrically-neutral. The first generation consists of the electron (e), the most commonly-found lepton forming shells around nuclei to create atoms and being responsible for electric current, and its corresponding neutrino, the electron neutrino (ν_e). The second generation consists of the muon (μ) and its corresponding neutrino, the muon neutrino (ν_μ). Muons are heavier than electrons and decay primarily into an electron, a muon neutrino, and an electron antineutrino. The mean lifetime of a muon is about $2 \mu\text{s}$ (in the reference frame of the muon). The third generation consists of the tau (τ) and its corresponding neutrino, the tau neutrino (ν_τ). Taus are heavier still and can decay either leptonically (into a tau neutrino, an electron (muon), and an electron (muon) antineutrino), or hadronically (into a tau neutrino and a quark-antiquark pair). The mean lifetime of a tau is about $3 \times 10^{-13}\text{s}$ (in the reference frame of the tau).

The bosons act as the force carriers of the SM. The photon (γ) mediates the electromagnetic interaction, the gluon (g) mediates the strong interaction, and the W and Z bosons mediate the weak interaction. The W can have electric charge +1 (W^+) or -1 (W^-), while the Z, photon, and gluon are all electrically neutral. The W and Z are also massive, while the photon and gluon are each massless. These bosons, known as gauge bosons or vector bosons, each have spin 1. The final boson, the scalar (spin 0) Higgs boson, is the final boson in the Standard Model and is responsible for mediating the Higgs field (discussed further in the section on the Higgs mechanism).

3.2 Quantum Electrodynamics

Quantum electrodynamics (QED) describes the interactions between particles having electric charge and the photons which mediate the electromagnetic force. A massive, unconstrained, fermionic field $\psi(x)$ with mass m (such as an electron) may be described according to the Dirac Langrangian:

$$\mathcal{L}_{\text{Dirac}} = i\bar{\psi}\gamma^\mu(\partial_\mu + ieA_\mu) - m\bar{\psi}\psi \quad (3.1)$$

where the γ^μ are Dirac matrices representing Lorentz transformations on the Dirac spinors ψ , and the A_μ correspond to the photon field. This Lagrangian corresponds to observable fields, so it must be invariant under gauge transformations. $\psi(x)$ is invariant under Lorentz transformations, and we define it to be invariant under the transformation

$$\psi(x) \rightarrow e^{ie\alpha(x)}\psi(x) \quad (3.2)$$

where e is the electron charge ($\approx 1.6 \times 10^{-19}$ Coulombs) and $\alpha(x)$ is some position-dependent angle.

To transform $\psi(x)$ in position to $\psi(y)$, we define the scalar operator $U(x, y)$ such that

$$\psi(y) = U(x, y)\psi(x) \quad (3.3)$$

If we take the transformation to be infinitesimally small, we have

$$y = x + \epsilon n^\mu \quad (3.4)$$

If we expand this, we get

$$U(x, x + \epsilon n^\mu) = 1 - \epsilon en^\mu A_\mu + O(\epsilon^2). \quad (3.5)$$

In order for the Lagrangian to remain invariant, we must have

$$A_\mu(x) \rightarrow A_\mu(x) - \frac{1}{\epsilon} \partial_\mu \alpha(x). \quad (3.6)$$

Now, if we define

$$D_\mu \equiv \partial_\mu + ieA_\mu \quad (3.7)$$

we can construct the commutator

$$[D_\mu, D_\nu] \psi(x) = (D_\mu D_\nu - D_\nu D_\mu) \psi(x) = ie (\partial_\mu A_\nu - \partial_\nu A_\mu) \psi(x) \equiv ie F_{\mu\nu} \psi(x) \quad (3.8)$$

which allows our Lagrangian to be fully gauge invariant. Note that there is no mass term $A_\mu A_\mu$, ensuring that the photon is massless. Putting everything together, we arrive at the final Lagrangian for QED:

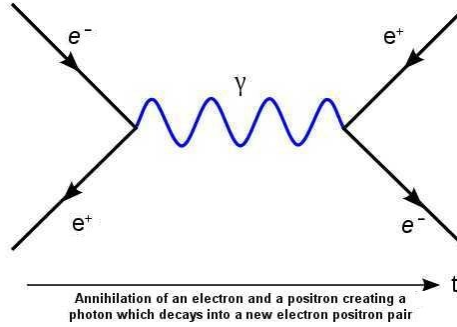


Figure 3.2: Typical QED interaction

$$\mathcal{L}_{\text{QED}} = \bar{\psi} i(\gamma^\mu D_\mu - m) \psi - \frac{1}{4} F_{\mu\nu} F^{\mu\nu}. \quad (3.9)$$

A typical QED interaction, an electron-positron pair annihilating into a photon which then decays into another electron-positron pair, is shown in Figure 3.2.

3.3 Electroweak Theory

The weak force is responsible for radioactive decay and is mediated by the W and Z bosons. It is perhaps best understood in terms of its unification with electromagnetism known as Electroweak theory. Both quarks and leptons can interact via the weak force, with W and Z bosons decaying to both.

The symmetry group of EW theory is $SU(2)_L \times U(1)_Y$, where $SU(2)_L$ is non-Abelian with generators $I_i = \sigma_i$ where σ_i are the standard Pauli matrices, and where $U(1)_Y$ is Abelian with generator $Y/2 = Q - I_3$ where Q is the electric charge. The corresponding gauge bosons are the W_1 , W_2 , and W_3 from $SU(2)_L$, and the B from $U(1)_Y$ and are all massless. Through spontaneous symmetry breaking via the Higgs mechanism, these four massless bosons become the massive W^\pm and Z and the massless photon of the SM.

Before electroweak symmetry breaking, the EW Lagrangian is defined to be

$$\mathcal{L}_{EW} = -\frac{1}{4}W_{\mu\nu}^i W_i^{\mu\nu} - \frac{1}{4}B_{\mu\nu}B^{\mu\nu} + \bar{f}_L \gamma^\mu \left(i\partial_\mu - \frac{g}{2}\sigma_i W^i - g'\frac{Y}{2}B_\mu \right) f_L + \bar{f}_R \gamma^\mu \left(i\partial_\mu - g'\frac{Y}{2}B_\mu \right) f_R \quad (3.10)$$

where we define:

$$W_{\mu\nu}^i \equiv \partial_\mu W_\mu^i - \partial_\nu W_\mu^i - g\epsilon_{ijk}W_\mu^j W_\nu^k \quad (3.11)$$

and

$$B_{\mu\nu} \equiv \partial_\mu B_\nu - \partial_\nu B_\mu. \quad (3.12)$$

Here, g and g' are the respective coupling constants for $SU(2)_L$ and $U(1)_Y$, and f_R and f_L represent right- and left-handed fermionic fields, respectively. “Handedness”, or helicity, is simply the dot product of the momentum and spin unit vectors of the particle. Right-handed particles have helicity +1, and left-handed particles have helicity -1.

After spontaneous symmetry breaking, the massless W_1 and W_2 combine to form the massive W^\pm via the relation

$$W^\pm = \frac{1}{\sqrt{2}}(W_1 \mp iW_2) \quad (3.13)$$

and the massless B and W_3 combine to form the massive Z and massless photon via the relation

$$\begin{pmatrix} \gamma \\ Z \end{pmatrix} = \begin{pmatrix} \cos \theta_W & \sin \theta_W \\ -\sin \theta_W & \cos \theta_W \end{pmatrix} \begin{pmatrix} B \\ W_3 \end{pmatrix} \quad (3.14)$$

where θ_W is the weak mixing angle, which defines the rotation by which spontaneous symmetry breaking transforms the $W_{1,2,3}$ and B into the W^\pm , Z , and photon of the SM. In terms of the coupling constants of $SU(2)_L$ and $U(1)_Y$, the weak mixing angle may be defined as:

$$\cos \theta_W = \frac{g}{\sqrt{g^2 + g'^2}} \quad (3.15)$$

and empirically as

$$\cos \theta_W = \frac{m_W}{m_Z}. \quad (3.16)$$

3.4 Quantum Chromodynamics

Quantum chromodynamics (QCD) is the theory that describes the strong force. QCD introduces a new property, called “color,” that is only felt by particles which strongly interact. These particles are quarks (q , the constituents of baryons and mesons) and gluons (g , the mediator of the strong force). Particles can have color charge “red”, “green”, or “blue” according to rotations in the group $SU(3)_C$, the portion of the SM relevant to QCD.

The generators of $SU(3)$ are eightfold, and can be used to represent the gauge transformation $U(\alpha)$:

$$U(\alpha) = e^{i\alpha_j T^j} \approx I + i\alpha_j T^j + O(\alpha^2) \quad (3.17)$$

They satisfy the commutation relation:

$$[T^a, T^b] = if^{abc}T^c \quad (3.18)$$

where

$$f^{abc} \equiv -2i\text{Tr} \left(T^a T^b T^c - T^b T^a T^c \right). \quad (3.19)$$

We can write the Lagrangian of QCD as:

$$\mathcal{L}_{\text{QCD}} = -\frac{1}{4}F_{\alpha}^{\mu\nu}F_{\mu\nu}^{\alpha} + \bar{q}(i\gamma^{\mu}D_{\mu} - m)q - \frac{1}{2\xi}\partial_{\mu}A^{\alpha\mu}\partial_{\nu}A^{\alpha\nu} + \partial_{\mu}\bar{c}^a \left(\partial^{\mu}\delta^{ab} + g_s f_{abc}A^{c\mu} \right) c_b. \quad (3.20)$$

Here, we define

$$D_{\mu} \equiv \partial_{\mu} + ig_s A_a^{\mu}T^a \quad (3.21)$$

and

$$F_{\mu\nu}^\alpha \equiv \partial_\mu A_\nu^\alpha - \partial_\nu A_\mu^\alpha - g_s f^{abc} A_\mu^b A_\nu^c \quad (3.22)$$

where g_s is the coupling constant of the strong force and A^μ represents the gluon field. The first term in the Lagrangian represents the gluon propagator, but note that it also includes a gluon self-interaction. This is in contrast to the QED Lagrangian, which allows no photon self-interaction. Due to this, QCD in fact allows for a bound state made entirely of gluons known as a “glueball,” although none have been experimentally observed. The second term represents the quark-gluon interactions as well as the free quark propagator. The final two terms are required to keep the Lagrangian gauge-invariant.

No stable particle may have non-neutral overall color charge. Since quarks and gluons on their own have net color charge, they immediately pull quarks and gluons out of the vacuum in order to form color-neutral bound states. These bound states may either achieve color neutrality in the form of a quark-antiquark pair (e.g. red + antired = color-neutral), or as a three-quark baryon (red + green + blue = color-neutral). This process of pulling strongly-interacting particles out of the vacuum is called *hadronization*. Hadronization occurs because the strong force is extremely short-ranged (on the order of a proton radius). As two color-charged particles are pulled apart, the energy required to keep them in a bound state satisfying color-neutrality increases rapidly. Very quickly, it becomes energetically favorable to pull a quark-antiquark pair out of the vacuum to form new color-neutral states. This requirement of color-neutrality is called *color confinement*, and the property of the strong coupling strength increasing rapidly with distance is known as *asymptotic freedom*.

3.5 Spontaneous Symmetry Breaking and the Higgs Mechanism

Recall from 3.3 that, although the gauge bosons of the electroweak interaction, the $W_{1,2,3}$ and the B , are required by gauge invariance to be massless, some of their SM counterparts, the W^\pm

and Z , are observed to be massive (80.4 GeV and 91.2 GeV, respectively). In order for these bosons to retain their mass without violating the gauge symmetry, the Higgs mechanism was introduced to explain this spontaneous symmetry breaking.

Developed by Peter Higgs in 1964, the Higgs mechanism introduces an extra potential term $V(\Phi)$ into the EW Lagrangian, where

$$\Phi \equiv \begin{pmatrix} \phi^+ \\ \phi^0 \end{pmatrix}_L \quad (3.23)$$

and

$$V(\Phi) \equiv \mu^2 \Phi^\dagger \Phi + \lambda \left(\Phi^\dagger \Phi \right)^2. \quad (3.24)$$

The total addition to the EW Lagrangian is of the form

$$\mathcal{L}_{Add} = D_\mu \Phi^\dagger D^\mu \Phi - V(\Phi) \quad (3.25)$$

Minimizing the potential $V(\Phi)$ in Φ gives the vacuum expectation value (VEV) of Φ . If we choose $\mu^2 < 0$, we arrive at multiple critical points in our minimization and a degenerate state is possible. The VEV takes the form

$$\langle 0 | \Phi | 0 \rangle = \begin{pmatrix} 0 \\ \frac{\mu^2}{\sqrt{2}\lambda} \end{pmatrix}. \quad (3.26)$$

This VEV has infinite degenerate minima all with the same magnitude but different phase. Choosing one phase leads to spontaneous symmetry breaking, and the W and Z bosons acquire mass via

$$m_W = \frac{g}{2} \frac{|\mu^2|}{\lambda} \quad (3.27)$$

$$m_Z = \frac{m_W}{\cos \theta_W}. \quad (3.28)$$

The final piece of the SM, the Higgs boson, has a mass which is dependent entirely on the VEV:

$$m_H = \sqrt{2}|\mu^2|. \quad (3.29)$$

In July 2012, the Higgs boson was discovered concurrently by the ATLAS and CMS collaborations, and was measured to have a mass of 125.4 GeV.

Chapter 4

Beyond the Standard Model

As mentioned in the introduction, some of the most pressing questions in particle physics are the following: (1) What is the origin of the matter-antimatter asymmetry?; (2) What is the origin of neutrino mass?; (3) Are there new fundamental forces in nature?; (4) What is the origin of dark energy; and (5) Is the Higgs boson solely responsible for electroweak symmetry breaking and the origin of mass? Much like the Higgs mechanism is introduced to account for the $SU(2)\times U(1)$ symmetry breaking, there are a plethora of theoretical models which incorporate additional gauge fields and interactions to address these questions.

For example, string theory is considered a promising candidate for describing gravitational systems at strong coupling and thus plays a prominent role in the description of black holes and evolution of the universe through the understanding of the origin of dark energy. Similarly, models with additional neutrino fields at the TeV scale provide a possible explanation for the mass of light neutrinos. Such models often manifest themselves as new heavy particles that could be observed at the LHC. Surprisingly, some of these new particles predicted on the basis of pure particle physics arguments can even provide the correct dark matter relic density.

There are several ways new heavy gauge bosons appear. The most natural possibility is one in which these heavy gauge bosons are the gauge field of a new local broken symmetry. Examples include models with a new $U(1)$ gauge symmetry, little Higgs models, and E6 Grand Unified Theories (GUT). In models with a new $U(1)$ gauge symmetry, the Z' is the gauge boson of the broken symmetry. In little Higgs models, breaking of the global symmetry by gauge and Yukawa

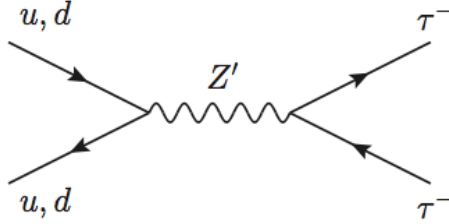


Figure 4.1: $Z' \rightarrow \tau\tau$ event at the LHC, wherein two quarks from colliding protons form a Z' which then decays to an oppositely-charged, back-to-back pair of τ leptons.

interactions generates Higgs mass and couplings at the TeV scale that cancel off the SM quadratic divergence of the Higgs mass from top, gauge, and Higgs loops. This results in one or more Z' bosons. In Kaluza-Klein models, the Z' bosons are excited states of a neutral, bulk gauge symmetry. From the breadth, scope, and implications of these models, it is apparent that probing these questions and puzzles potentially lies in the physics of new particles at the TeV scale. As such, it is highly worthwhile to engage in searches for Z' candidates.

Of particular interest such searches are models that include an extra Z' -like neutral gauge boson that decays to pairs of high- p_T τ leptons. Although many models with extra gauge bosons obey the universality of the couplings, some models include generational dependent couplings resulting in extra neutral gauge bosons that preferentially decay to τ leptons, making this analysis an important mode for discovery. However, even if a new gauge boson decaying to $\mu\mu$ is discovered first, it will be critical to establish the $\tau\tau$ decay channel to establish the coupling relative to $\mu\mu$ channel. The primary model studied in this thesis is the Sequential Standard Model Z' , denoted Z'_{SSM} . This model assumes universality of the couplings (just like the SM Z) which makes it a useful benchmark, both for testing other models and for fine-tuning the search methodology.

In pp collisions at the LHC, the Z'_{SSM} is expected to be generated in much the same way as the SM Z , through Drell-Yan production via quark-quark interactions from the colliding protons. A diagram of this process is shown in Figure 4.1.

Chapter 5

The Compact Muon Solenoid (CMS) Experiment

The CMS Experiment is a multipurpose particle detector located on the LHC ring underneath the Franco-Swiss border at CERN in Geneva, Switzerland. An overview of the experiments on the LHC ring can be seen in Figure 5.1. The experiment is located 100 meters underground in Cessy, France. CMS is 28.7 meters long, 15.0 meters in diameter, and weighs approximately 14,000 tonnes. It's arranged in a cylindrical, multi-layered structure consisting of a "barrel" and two endcaps, with the LHC beam passing through the vertical axis of the cylinder. CMS consists of several subdetectors, each designed to measure a different class or property of particle. From the beam line outward, the layers of CMS are the tracker, the electromagnetic calorimeter (ECAL), the hadronic calorimeter (HCAL), the superconducting solenoid, and the muon system (interspersed with the steel return yoke). A photograph of CMS can be seen in Figure 5.2.



Figure 5.1: The Large Hadron Collider located underneath the Franco-Swiss border at CERN near Geneva, Switzerland. The CMS Experiment is located on the French side in Cessy, France

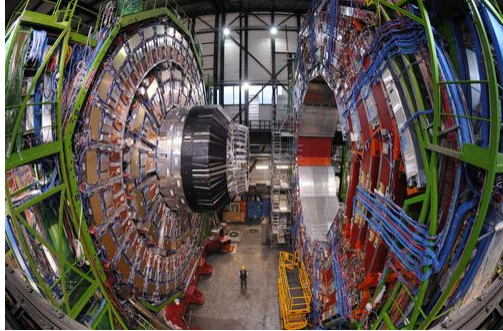


Figure 5.2: The CMS Experiment (open for maintenance)

The experiment uses a right-handed coordinate system: the origin is set at the pp collision point, with the x -axis pointing towards the center of the LHC ring, the y -axis pointing straight up, and the z -axis pointing along the beam line in the counter-clockwise direction. CMS also uses a pseudo-polar coordinate system, with θ defined as the polar angle from the beam axis, and η as the "pseudorapidity", itself defined as

$$\eta = -\ln [\tan (\theta/2)] \quad (5.1)$$

A diagram highlighting the layout of CMS can be seen in Figure 5.3.

5.1 The silicon tracker

The silicon tracker is the innermost detector element in CMS, and is designed to offer the highest resolution measurement of charged particle trajectories (such trajectories are referred to as "tracks"). The tracker is composed of approximately 200m^2 of silicon, and includes arrays of silicon pixels in the inner layer and arrays of silicon strips in the outer layer. The silicon elements are arranged in the densest configuration near to the interaction vertex ($r \approx 10\text{cm}$), with pixel size $\approx 100 \times 150\mu\text{m}^2$. As one moves away from the interaction vertex, the solid angle becomes large enough that the particle flux drops off to a degree that larger silicon elements may be used (silicon

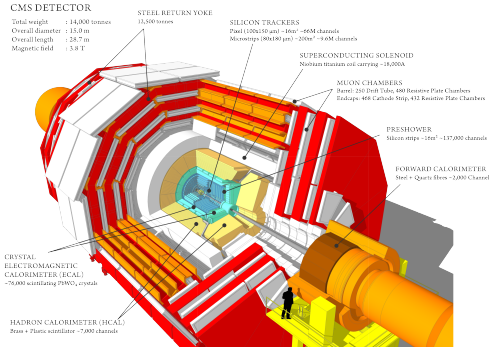


Figure 5.3: Schematic of the CMS Experiment showing the silicon trackers, electromagnetic calorimeter (ECAL), hadronic calorimeter (HCAL), superconducting solenoid, steel return yoke, and muon system.

strips measuring $10\text{cm} \times 80\mu\text{m}$ at $20\text{cm} < r < 55\text{cm}$, silicon strips measuring $25\text{cm} \times 180\mu\text{m}$ for $r > 55\text{cm}$. The total number of silicon elements is 66 million pixels and 9.6 million strips. The tracker is divided into a barrel segment and two forward endcaps. The endcaps contain two pixel and nine strip layers each, and the barrel segment is separated into an inner and outer barrel. A schematic of the tracker layout can be seen in Figure 5.4. Particle tracks are reconstructed from hits in the individual silicon pixels/strips, the track being interpolated between hits.

5.1.1 The pixel detector

The pixel detector, shown in Figure fig(PixelLayout), consists of three barrel layers and two endcap layers. The barrel has a length of 53 cm, and the endcap disks range from 6 cm to 15 cm in radius. The pixel modules are arranged in a ladder-like configuration in the barrel, with 768 total modules comprising the barrel. The endcap disks are arranged in a turbine-like fashion, with 24 "blades" per disk, and 7 pixel modules per blade for a total of 672 pixel modules in the endcaps. Each pixel consists of a readout chip (ROC), which are bump bonded to the modules. In total, the pixel detector includes about 16,000 ROCs.

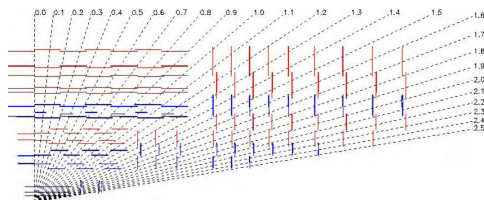


Figure 5.4: Overview of the silicon tracker layout.

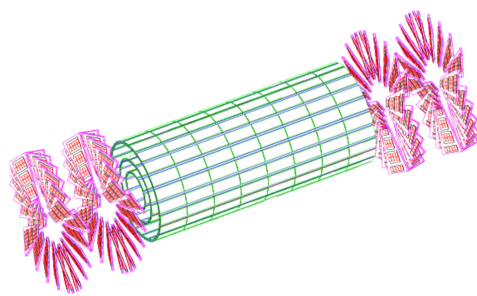


Figure 5.5: Diagram indicating the layout of the barrel pixel (BPIX) sensors (in green) and endcap pixel (FPIX) sensors (in pink)

5.1.2 The strip tracker

The strip tracker is divided into a barrel segment and two endcap segments. The barrel segment is itself divided into a Tracker Inner Barrel (TIB) section and a Tracker Outer Barrel (TOB) section. The TIB includes four layers of silicon strips each $320\mu\text{m}$ thick and ranging in pitch from $80\mu\text{m}$ and $120\mu\text{m}$. In the TOB, the lower rate of particle flux allows for larger strips (each $500\mu\text{m}$ thick and ranging in pitch from $120\mu\text{m}$ to $180\mu\text{m}$).

The endcaps are each comprised of a Tracker Endcap (TEC) and Tracker Inner Disks (TIDs). The TIDs are designed to fill the region between the TEC and the TIB. The TECs each contain nine disks, and each TID contains three disks. On each disk, the modules (for both TID and TEC) are arranged in rings centered on the beam line. The TID strips (and three innermost ring strips of the TEC) have thickness $320\mu\text{m}$, while the rest of the TEC strips have thickness $500\mu\text{m}$. In total the strip tracker contains about 15,400 strip modules.

5.2 The electromagnetic calorimeter

The next layer outward from the silicon tracker is the electromagnetic calorimeter (ECAL), which is designed primarily to measure energies of photons and electrons. The ECAL consists of an array of about 75,000 lead tungstate (PbWO_4) crystals, and has a barrel (BE) segment as well as two endcap (EE) segments. The BE segment has 61,200 crystals, while each EE segment contains 7,324 crystals.

PbWO_4 was chosen for the ECAL due to its short radiation length ($X_0 = 0.89\text{ cm}$), fast response time (80% of light emitted within 25ns), and radiation hardness (up to 10 Mrad).

The barrel (EB) crystals present an apparent cross-section (when viewed from the interaction vertex) of $\approx 22 \times 22\text{ mm}^2$, and are 230 mm (25.8 radiation lengths) thick. The barrel has an inner radius of 129 cm, and covers the pseudorapidity range $0 < |\eta| < 1.479$.

The endcap (EE) crystals are each arranged in two D-shaped semicircular aluminum plates. From these plates are cantilevered "supercrystal" structures consisting of 5x5 crystal blocks. Each

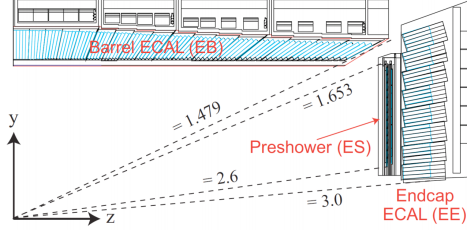


Figure 5.6: Layout of the electromagnetic calorimeter (ECAL) indicating the configuration of the barrel (EB) and endcap (EE) crystals.

crystal presents an apparent cross-section of $\approx 28.6 \times 28.6 \text{ mm}^2$, and are 220 mm (24.7 radiation lengths) thick, and the endcap crystals cover the pseudorapidity range $1.479 < |\eta| < 3.0$.

A diagram of the ECAL layout can be seen in Figure 5.6.

5.3 The hadronic calorimeter

Surrounding the ECAL is the hadronic calorimeter (HCAL). The primary function of the HCAL is to measure the energies of hadrons (particles made of quarks and gluons). Located just inside the solenoid magnet, the HCAL is primarily composed of brass panels made from melted-down artillery shells. Interspersed with the brass panels are plastic scintillation panels, in which are embedded wavelength-shifting (WLS) fibers, which carry the signal to clear fibers outside the scintillators for readout. As hadrons enter the HCAL, they produce secondary particles in the brass which in turn create further particles. These hadron "showers" then interact with the plastic scintillators, where the fibers carry the signal to hybrid photodiodes so the signal can be measured.

HCAL is divided into barrel (HB) and endcap (HE) portions. Due to limited space between the ECAL and solenoid, the HCAL also includes material outside the solenoid: the outer HCAL (HO) lining the solenoid, and the forward calorimeter (HF) outside the muon endcap system. These additions increase the total radiation lengths covered by the HCAL to 10.

While HB and HE use the brass-plastic configuration, HO uses the solenoid itself instead of the brass, although the same plastic scintillators are used. The HF uses steel in place of brass, and quartz fibers in place of plastic scintillators. This is done to preferentially select neutral

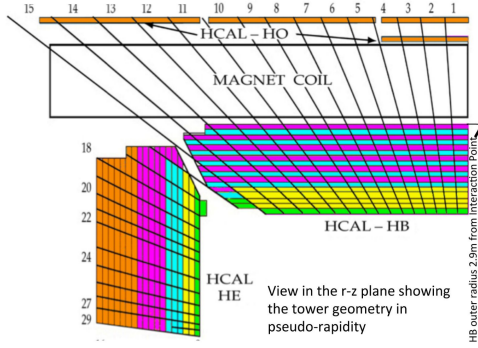


Figure 5.7: Layout of the hadronic calorimeter (HCAL) indicating the configuration of the barrel (HB) and endcap (HE) components as well as the outer HCAL (HO) lining the solenoid.

components of hadron showers, which are shorter and narrower and are thus well suited for the forward environment, which tends to be quite congested with particles.

A diagram of the HCAL layout is shown in Figure 5.7.

5.4 The CMS magnet

The need to measure high p_T muons has driven the requirements on the CMS magnetic field strength. With the goal to accurately determine both momentum and sign of 1TeV muons at $\Delta p/p \approx 10\%$, a superconducting solenoid with an interior magnetic field strength of 3.8T was chosen as the central design feature of CMS.

The solenoid is located outside the silicon tracker, ECAL, and HCAL systems but inside the muon system. Interspersed with the muon system is the steel return yoke, which contains the field outside the solenoid and provides a 2T field to allow the muon system to measure charged particle momentum.

To generate the magnetic field, 18,160 amperes are passed through four layers of tightly-wound superconducting Nb-Ti wire, resulting in a stored energy of 2.3 gigajoules.

The magnetic field generated by the solenoid bends charged particles according to the equation

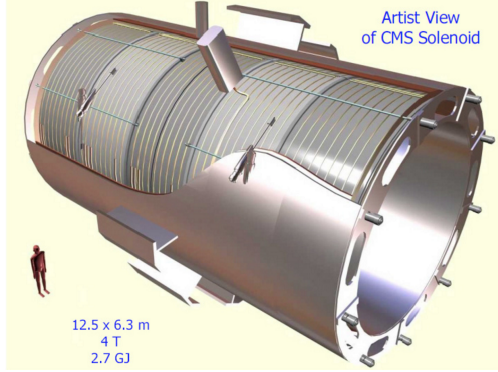


Figure 5.8: The superconducting solenoid.

$$R = \frac{p_T}{0.3eB}$$

where R is the radius of curvature (in meters), p_T is the transverse momentum (in GeV), e is the electron charge (in Coulombs), and B is the field strength (in Tesla). Thus, the transverse momentum (p_T) of the charged particle can be measured from the known field strength and the observed radius of curvature of the tracks measured in the tracker and muon systems.

An artist's rendition of the superconducting solenoid can be seen in Figure 5.8.

5.5 The muon system

The muon system is the outermost subdetector, and is central to the design of CMS. It is composed of three separate sensor elements: drift tubes (DTs), cathode strip chambers (CSCs), and resistive plate chambers (RPCs). A diagram of one quadrant of the muon system can be seen in Figure fig(muonSystemLayout). "MB" indicates the muon barrel subdetector, which is composed of DTs, "RB" indicates the RPC barrel subdetector, "ME" indicates the muon endcap subdetector (CSCs), and "RE" indicates the RPC endcap subdetector.

An overview of the layout of the muon system can be seen in Figure 5.9

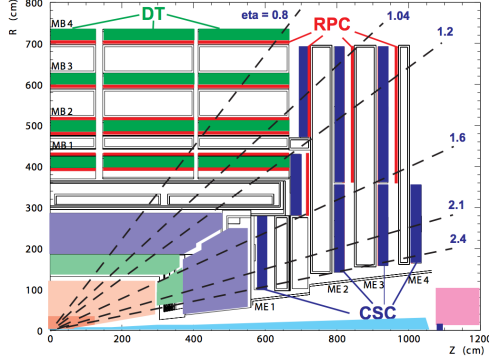


Figure 5.9: Layout of the muon system highlighting the layered structure of the drift tubes (DTs, green), cathode strip chambers (CSCs, blue), and resistive plate chambers (RPCs, red).

5.5.1 Drift tubes (DTs)

The barrel of the muon system contains 250 layers of DTs arranged in four layers (labeled MB1, MB2, MB3, and MB4 in Figure fig(muonSystemLayout)). In the MB1, MB2, and MB3 layers, DTs are arranged in 8 $r - \phi$ -measuring planes, and 4 z -measuring planes. The MB4 layer only contains $r - \phi$ -measuring planes.

Each DT is filled with a gaseous mixture of Argon (85%) and carbon dioxide (15%). Charged particles passing through the DT will ionize the gaseous mixture and produce a current along a central filament to be read out. The maximum drift length per DT is 2.0cm and the single point resolution is $\approx 200 \mu\text{m}$.

5.5.2 Cathode strip chambers (CSCs)

The muon endcap (ME) system is comprised of 234 CSCs in each endcap. The CSCs are trapezoidal in shape and are arranged in four layers (labeled ME1, ME2, ME3, and ME4 in Figure fig(muonSystemLayout)). The innermost layer (ME1), is made of 108 CSCs arranged in three rings of 36 CSCs each. The other layers each have two rings (18 CSCs on the inner ring, 36 on the outer ring, for a total of 54 CSCs per layer).

Each CSC is comprised of six gas gaps, with each gap containing a radial array of cathode strips and a plane of anode wires running perpendicular to the cathodes. The CSCs are overlapped

in ϕ to avoid gaps in the particle acceptance. When a charged particle ionizes the gas, it leaves a charge on the anode wire and an image charge on a group of cathode strips. The spatial resolution provided from each CSC is $\approx 200\mu\text{m}$.

The forward (endcap) region of the muon system can expect a higher muon flux, so CSCs were chosen due to their fast response time and fine resolution.

5.5.3 Resistive plate chambers (RPCs)

RPCs can be found in both the barrel and endcaps of the muon system, and are used in parallel with the other two subsystems. The RPCs have timing resolution on the order of nanoseconds and are used primarily to resolve ambiguities in cases of multiple hits in the DTs or CSCs, thereby improving the overall accuracy of particle reconstruction.

There are two layers of RPCs "sandwiching" each of the first two DT layers (MB1 and MB2), while the outer DT layers (MB3 and MB4) are paired with one RPC each. The endcap CSCs are also paired with one RPC each.

Each RPC is comprised of parallel plates of bakelite enclosing two millimeter-thick gas gaps. Each gas gap contains a mixture of 96.2% R134a ($\text{C}_2\text{H}_2\text{F}_4$), 3.5% isobutane (C_4H_{10}), and 0.3% sulfur hexafluoride (SF_6).

5.6 The trigger system

When running at full luminosity, the LHC generates pp collisions at a rate of 40MHz. With each event requiring $\approx 10\text{MB}$ of digital storage space, this equates to a data-generation rate of 400TB per second. Since this is obviously unsustainable with current computer storage technology, CMS employs a trigger system to reduce the rate of stored events. Two levels of triggering are used: the hardware-based Level-1 (L1) trigger, which reduces the rate from 40MHz to approximately 100kHz, and the hardware-and-software-based High Level Trigger (HLT), which reduces the rate from $\approx 100\text{kHz}$ to 300Hz.

5.6.1 The Level-1 (L1) trigger)

The L1 trigger takes data from the muon system, HCAL, and ECAL in order to make a rapid decision about whether or not to keep the event and send it to the HLT for further review. The L1 triggering rate is about $3.2\mu\text{s}$, during which time the entirety of the data from the event is temporarily stored. Information from the silicon tracker is not used in this stage of triggering, as the time required by the tracker to reconstruct a track is outside this triggering time window.

The L1 trigger is divided into three major components: the calorimeter trigger, the muon trigger, and the global trigger. The calorimeter trigger looks at the combined (summed) energy deposits in ECAL and HCAL. If the sum is greater than a given threshold, an "accept" signal is sent to the global trigger. The muon trigger looks at the DTs, CSCs, and RPCs which in conjunction form the muon system. If they in concert report at least four muons, each having high transverse momentum and high-resolution tracks ("good"-quality muons), an "accept" signal is sent to the global trigger. The global trigger makes the final decision to reject the event or, if it has received "accept" signals from both the calorimeter trigger and muon trigger, to send it to the HLT.

5.6.2 The High level trigger (HLT)

The HLT is software-based and uses software-defined "HLT paths" in order to determine whether or not a given event will pass a particular physics object selection determined by the path. The advantage of this setup is that different HLT paths can be used by different analysis groups looking for different physics signatures.

The HLT first reconstructs the entirety of the event from the stored data passed to it by the L1 trigger, and determines whether the event passes a given trigger path. There are four broad categories of HLT path: electrons/photons and muons, jets, missing transverse energy (\cancel{E}_T), and taus. Hundreds of specific paths offering high levels of discrimination between required selection criteria are available and grouped into these four categories. As the paths are software-based and not hardware-based, new paths can be customized to the needs of any analysis effort.

In order to determine whether or not an event passes a given path, the entire event is reconstructed and run through three broad triggering steps: Stage 2 (calorimetry), Stage 2.5 (calorimetry+pixel hits), and Stage 3 (full reconstruction). In Stage 2, a threshold on calorimeter energy is applied. An object must have a combined ECAL+HCAL calorimetry energy greater than the threshold specified by the path in order to move on to Stage 2.5. In Stage 2.5, information from the pixel subdetector in the silicon tracker is used in order to verify that the hits recorded in the calorimetry towers have corresponding tracks in the pixel system (assuming the particle in question is charged). Finally, in Stage 3, information from the entire detector is used to reconstruct the entirety of objects in the event and ensure that they pass momentum, energy, and quality criteria specified by the path.

5.7 Particle Reconstruction

Even after a given event has passed the L1 trigger and HLT requirements, its constituent particles only exist as hit patterns in the various subdetectors of CMS. In order for any kind of meaningful physics analysis to be performed, these hit patterns must be turned into physics objects which are more easily-read by the CMS software framework (CMSSW). Broadly, the six principle objects that are "reconstructed" from raw detector data in this manner are: electrons, muons, taus, photons, jets, and missing energy (\cancel{E}_T). The chief set of software tools used to reconstruct physics objects is a group of algorithms collectively referred to as Particle Flow (PF).

5.7.1 Particle Flow

Particle Flow (PF) is the term used to refer to the general set of algorithms used to reconstruct physics objects (particles) out of raw detector data. The fundamental inputs to the PF algorithms are the charged particle tracks (from the silicon tracker), hits in the calorimetry towers (from ECAL and HCAL), and hits in the muon system. These fundamental inputs are then grouped into "blocks" which the PF algorithm translates into physics objects. Muons are identified by matching a track in the tracker with a hit in the muon system, charged hadrons are identified by matching

a track in the tracker with a hit in HCAL, and electrons are identified by matching a track in the tracker with a hit in ECAL. Photons and neutral hadrons leave no tracks, so they are identified as hits in ECAL and HCAL, respectively, with no matching tracks. As tracks are matched with calorimetry towers and muon hits, those hits are removed from consideration and whichever tower hits are leftover are assumed to be from photons or neutral hadrons. Once all the visible particles are reconstructed, conservation of momentum principles are applied to infer the missing energy, or E_T .

The following subsections will detail the methods used to reconstruct each class of particle, and a final subsection will detail the means by which the event data produced by Particle Flow is packaged into formats useful for analysis efforts.

5.7.1.1 Track reconstruction and vertexing

The goal of the silicon tracker is to reconstruct tracks indicating the trajectories of charged particles through the magnetic field, and furthermore to use these trajectories to “trace back” the origin of the particle, known as the vertex. The first vertex in each event, that corresponding to the pp collision, is known as the primary vertex (PV). The presence of multiple proton-proton collisions in each bunch crossing, a phenomenon known as pileup, presents the possibility of misidentifying the correct PV for a given event. Therefore, there is a need for a vertexing and tracking algorithms exhibiting a high degree of granularity.

To ensure this, tracks with the highest number of hits in the pixel and strip subsystems within the silicon tracker are recorded (and reconstructed) first. Tracks with three hits, high p_T , and close proximity to the beam spot are considered to be high quality. These tracks are reconstructed first, and their hits removed. For the remaining, lesser-quality tracks, looser criteria are applied iteratively until all tracker hits have been accounted for.

In order to determine the location of the PV, the reconstructed tracks are clustered together and the location is extrapolated by requiring that each track cluster share a plane compatible with the beam line. This is done online as well as offline so that the PV information can be relayed to

the HLT for use in the triggering process. The reconstruction algorithm uses only information from the pixel subdetector for the online reconstruction, while the offline reconstruction uses information from the entire tracker.

5.7.1.2 Electron reconstruction

Electrons are reconstructed via the combination of a track in the silicon tracker and hits in the ECAL towers. These tower hits are called “superclusters” and their size in η and ϕ is dictated by various clustering algorithms selected according to the relevant HLT path. As the electron interacts with the silicon in the tracker, it radiates photons via Bremsstrahlung. This emission causes the electron to bend further in the magnetic field. To account for this, the supercluster size is tuned to catch these Bremsstrahlung photons as well, thereby capturing the total energy of the electron before bending and leading to a more accurate calculation of the electron’s energy and momentum.

To fully reconstruct an electron track, one starts with a track **seed**, which is a possible electron trajectory found by interpolating between layer hits in the pixel and strip detectors. These track seeds must be cleaned and filtered in order to find the most likely track candidate, and then they must be matched with a supercluster in ECAL. There are two methods to achieve this. The first, ECAL driven seeding, begins by reconstructing superclusters in ECAL and attempts to match them with track seeds in the innermost layer of the pixel detector. The track is then reconstructed from these track seeds. The second, tracker driven seeding, begins with a high-quality track seed and attempts to match it to an appropriate supercluster in ECAL, while also taking into account other clusters arising from Bremsstrahlung photons. This is achieved by drawing straight lines tangent to the track towards the ECAL. If a corresponding cluster is found, it is added to the total energy of the electron.

5.7.1.3 Muon reconstruction

Muons can be measured both in the silicon tracker and the muon system. In order to reconstruct a muon, hits in the muon system (**stand-alone muons**) are matched to hits in the tracker in order to reconstruct a complete muon object, known as a **global muon**. These muons are reconstructed using two different methods, **global muon reconstruction (outside-in)** and **tracker muon reconstruction (inside-out)**.

Global muon reconstruction begins in the muon system. Hits in the DTs and CSCs are allocated into segments, which are short stubs containing just enough hits to assign each a momentum and direction vector. These segments are grouped together to form tracks in the muon system. These tracks, known as stand-alone muon tracks, are matched, one by one, with tracks from the tracker by comparing parameters of the two tracks propagated onto a common surface.

Tracker muon reconstruction begins in the silicon tracker. All tracks with $p_T > 0.5 \text{ GeV}/c$ and $p > 2.5 \text{ GeV}/c$ are considered possible muon candidates and are propagated outward toward the muon system, taking into account the magnetic field, expected energy loss, and the possibility for multiple Coulomb scattering in the detector material. If a hit in the muon system is found within 3 cm in local x, y coordinates, the candidate qualifies as a tracker muon.

Tracker muon reconstruction is more efficient than global muon reconstruction at low energies ($p < 5 \text{ GeV}/c$), since it only requires one muon segment in the muon system. Global muon reconstruction is more appropriate for muons with higher energies penetrating through more than one station in the muon system.

5.7.1.4 Photon and Neutral Hadron Reconstruction

Since photons and neutral hadrons are chargeless, and therefore leave no hits in the silicon tracker, the entirety of their reconstruction takes place in ECAL (photons) and HCAL (hadrons). The identification of photons and neutral hadrons takes place via so-called **clustering algorithms** which are designed to separate photons from neutral as well as charged hadrons, and to differen-

tiate photons originating from the primary or secondary decays from those generated by electrons undergoing Bremsstrahlung within ECAL.

Clustering algorithms involve three steps. First, a seed cluster is identified in one of the ECAL towers as a tower with a local energy maximum passing a threshold specified by the algorithm. Next, topological clusters are defined as clusters adjacent to (sharing at least one side in common with) the seed cluster and with cell energies passing another threshold. These thresholds are generally set to be two standard deviations above the base electronics noise level in each of the separate ECAL segments (80MeV in the barrel and 300MeV in the endcaps). Finally, topological clusters then generate as many “particle flow” clusters as there are seed clusters, and the energy in each particle flow cluster is allocated according to its distance from the seed.

Furthermore, in particle flow, ECAL/HCAL clusters are required **not** to match any tracks in the tracker in order to qualify as photon or neutral hadron candidates.

5.7.1.5 Jet Reconstruction

Jets are primarily reconstructed in ECAL and HCAL, although their charged constituents usually leave tracks in the silicon tracker as well. The majority of reconstructed jet energy comes from charged particles such as pions and kaons, and a smaller but still sizable portion comes from photons from π^0 decays in ECAL. Though numerous jet reconstruction algorithms exist, most jet candidates are reconstructed using the Particle Flow (PF) algorithm. The PF algorithm looks at the constituent particles in the jet: charged hadrons, neutral hadrons, and photons individually and then clusters them into jet candidates according to various clustering algorithms, the most common of which is the **anti- k_T** algorithm with a cone radius of $R = 0.5$. The energy of photons is determined from ECAL measurements, that of charged hadrons is measured with a combination of tracker, ECAL, and HCAL measurements, and the energy of neutral hadrons is measured according to the description in the previous section.

Approximately 90% of the reconstructed jet energy comes from charged hadrons and photons, while the remaining 10% comes from neutral hadrons. Since tracking information from the charged

hadrons is available, improved jet vertexing can be done and the impact of pileup can be mitigated.

Chapter 6

Results

6.1 13 TeV Results

Figure 6.1 shows the background predictions as well as the observed $m(\tau_1, \tau_2, \cancel{E}_T)$ spectrum, in log scale, for the four channels considered in this analysis note: $\mu\tau_h$ (top left), $\tau_h\tau_h$ (top right), $e\tau_h$ (bottom left), $e\mu$ (bottom right). Table ?? lists the number of estimated background events compared with the total number of observed events in data for each final state considering the whole mass spectrum, while Table ?? lists those considering $M(\tau_1, \tau_2, \cancel{E}_T) > 300$ GeV. The observed $m(\tau_1, \tau_2, \cancel{E}_T)$ spectrum in the signal region does not reveal any evidence for $Z' \rightarrow \tau\tau$ production

Process	$\tau_h\tau_h$	$\mu\tau_h$	$e\tau_h$	$e\mu$	
Drell-Yan	8 ± 3	882 ± 127	375 ± 118	321 ± 99	
W+jets	0.1 ± 0.1	916 ± 96	546 ± 86	19 ± 11	
Diboson	0.5 ± 0.5	29 ± 7	18.0 ± 4	108 ± 17	
$t\bar{t}$	–	26 ± 7	26 ± 8	223 ± 45	
Multijet	49 ± 13	122 ± 84	117 ± 72	32 ± 24	
Total	58 ± 13	1976 ± 180	1082 ± 162	703 ± 113	
Observed	55	1807	1113	728	

Table 6.1: Number of observed events in data and estimated background events for the whole mass range. The uncertainties quoted on the number of background events represent the combined statistical and systematic uncertainty.

An upper bound at 95% confidence level (CL) is set on $\sigma \cdot BR$, where σ is the cross-section for pair production of $pp \rightarrow Z'$ and BR the branching fraction for $Z' \rightarrow \tau\tau$.

The calculation of the exclusion limit is obtained by using each bin of the $m(\tau_1, \tau_2, \cancel{E}_T)$ distribution to construct one bin of the likelihood and computing the 95% confidence level (CL)

Process	$\tau_h \tau_h$	$\mu \tau_h$	$e \tau_h$	$e \mu$	
Drell-Yan	5 ± 2	16 ± 4	9 ± 3	4 ± 2	
W+jets	0.004 ± 0.004	23 ± 9	17 ± 7	1 ± 1	
Diboson	0.02 ± 0.02	6 ± 3	2 ± 1	23 ± 4	
$t\bar{t}$	–	4 ± 2	5 ± 1	65 ± 13	
Multijet	18 ± 6	4 ± 3	6 ± 2	1 ± 1	
Total	23 ± 6	51 ± 11	39 ± 8	94 ± 14	
Observed	20	42	40	96	

Table 6.2: Number of observed events in data and estimated background events in the region $M(\tau_1, \tau_2, \cancel{E}_T) > 300$ GeV. The uncertainties quoted on the number of background events represent the combined statistical and systematic uncertainty.

upper limit on the signal cross-section using the asymptotic CL_s method. Said differently, a shape based analysis is performed, using the $m(\tau_1, \tau_1, \cancel{E}_T)$ distribution as the fit discriminant to determine the likelihood of observing signal in the presence of the predicted background rate, given the observed yield in data. Systematic uncertainties are represented by nuisance parameters, which are profiled, assuming a log normal prior for normalization parameters, and Gaussian priors for mass-spectrum shape uncertainties.

The above procedure is performed using the Higgs limit calculation tool “combine”. The tool takes as input data cards with the yields and nuisance parameters in each $m(\tau_1, \tau_1, \cancel{E}_T)$ bin of the search channels. These data cards are provided by the four channels being considered, and the only further input that is required is the correlations within and across channels. As only an example, if all the channels had 10 bins from $0 < m(\tau_1, \tau_1, \cancel{E}_T) < 5000$ GeV (500 GeV/bin), this means there will be 10 cards per channel and therefore 40 cards in total for the four channels (if all the channels have the same bin size). The cards corresponding to a specific final state, e.g. $\mu \tau_h$, were then combined using the “CombineCards.py” tool provided by the Higgs limit tool, resulting in a single *combined* data card. This procedure was performed for all the final states considered in the analysis, resulting in X *combined* cards. The individual limits, per channel, were obtained by running the combine tool over each *combined* card separately. The final combined limit was obtained by combining the four resulting *combined* cards per channel described above, using the “CombineCards.py” tool. In order to handle correlations within and across channels, the following

approach was used. Each nuisance parameter was defined with a convention of two indices: the first index, i , denoted the channel ($i = \mu\tau_h = 0, i = \tau_h\tau_h = 1, i = e\tau_h = 2, i = e\mu = 3$) and the second one the type of process ($j = \text{Signal} = 0, j = \text{W+jets} = 1$, etc.). Since the limit tool handles nuisance parameters with the same name as fully correlated, correlations across channels and processes were specified by utilizing the same i and process index j , respectively.

Figure 6.1 shows the expected limits as well as the theoretical cross-section as functions of $m(Z')$ mass for each channel. Figure 6.4 show the combined limit. A k factor of 1.3 has been used to scale the leading order (LO) signal cross-section. We exclude Z' (decaying through $Z' \rightarrow \tau\tau$) masses below approximately 2.0 TeV.

Table 6.3: Event summary table after signal region selection

Process	$\tau_h\tau_h$	$\mu\tau_h$	$e\tau_h$	$e\mu$
Z' (500)	307.4 ± 35.3	502.3 ± 57.7	197.6 ± 22.7	218.6 ± 27.3
Z' (1000)	34.6 ± 2.6	40.8 ± 3.1	14.7 ± 1.1	19.0 ± 1.5
Z' (1500)	6.6 ± 0.3	7.2 ± 0.3	2.3 ± 0.1	3.6 ± 0.2
Z' (2000)	1.6 ± 0.07	1.8 ± 0.08	0.59 ± 0.03	0.91 ± 0.04
Z' (2500)	0.55 ± 0.02	0.60 ± 0.02	0.19 ± 0.01	0.30 ± 0.01
Z' (3000)	0.13 ± 0.01	0.14 ± 0.01	0.04 ± 0.00	0.07 ± 0.00
Drell-Yan	8.4 ± 3.1	882.4 ± 127.0	375.1 ± 117.6	321.2 ± 99.2
W+jets	0.1 ± 0.1	916.2 ± 96.1	545.8 ± 85.6	18.9 ± 11.4
Diboson	0.5 ± 0.5	29.2 ± 7.4	18.0 ± 4.4	108.3 ± 17.4
$t\bar{t}$	—	26.1 ± 6.7	26.1 ± 7.5	222.8 ± 44.8
Multijet	48.7 ± 13.0	121.8 ± 83.5	116.7 ± 71.5	31.9 ± 24.3
Observation	55	1807	1113	728

6.2 8 TeV Results

The search for $Z' \rightarrow \tau\tau$ events was also carried out during the 2012 run of the LHC, when the center-of-mass collision energy was lower at $\sqrt{s} = 8$ TeV. 19.7 fb^{-1} of collision data were collected during this run. Due to poor performance of the Tau POG recommended hadronic tau identification and reconstruction algorithms, the only channel which was studied to completion was the $e\mu$ channel. As the analysis strategy, trigger studies, and background estimation techniques were nearly identical to those presented for the $e\mu$ channel at $\sqrt{s} = 13$ TeV, only the results of the

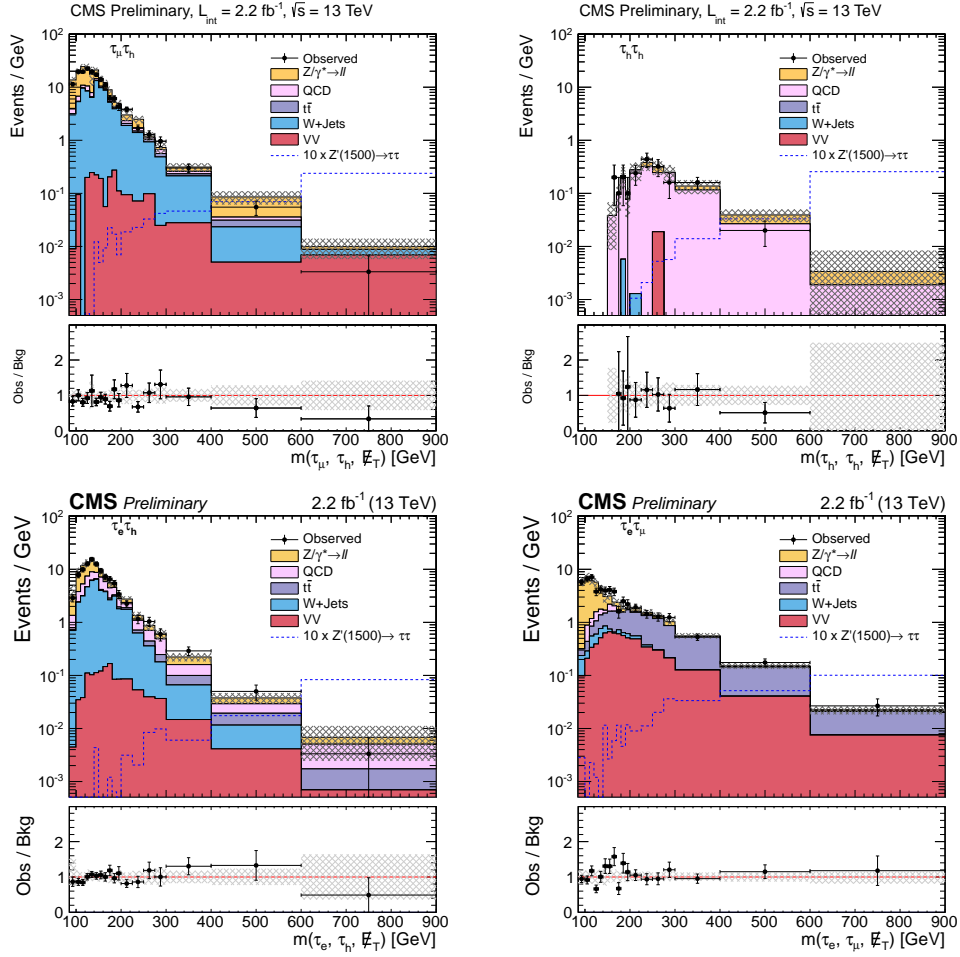


Figure 6.1: Top Left: $m(\mu, \tau_h, \cancel{E}_T)$ distribution in the signal region, in log scale. Top Right: $m(\tau_h, \tau_h, \cancel{E}_T)$ distribution in the signal region, in log scale. Bottom Left: $m(e, \tau_h, \cancel{E}_T)$ distribution in the signal region, in log scale. Bottom Right: $m(e, \mu, \cancel{E}_T)$ distribution in the signal region, in log scale.

8 TeV $e\mu$ analysis are shown here.

Figure 6.5 and Figure 6.6 show the unblinded signal region and background rates after all backgrounds are estimated. Data agrees with SM expectation, so limits are set on the Z'_{SSM} visible mass.

Figure 6.7 shows the predicted rates in the SR of several signal mass points considered in this analysis.

Finally, the limit on a Z'_{SSM} decaying to two taus are given in Figure 6.8. Upper limits are placed on $\sigma(pp \rightarrow Z') \times BR(Z' \rightarrow \tau\tau)$ as a function of mass. The limit is set as the point at which

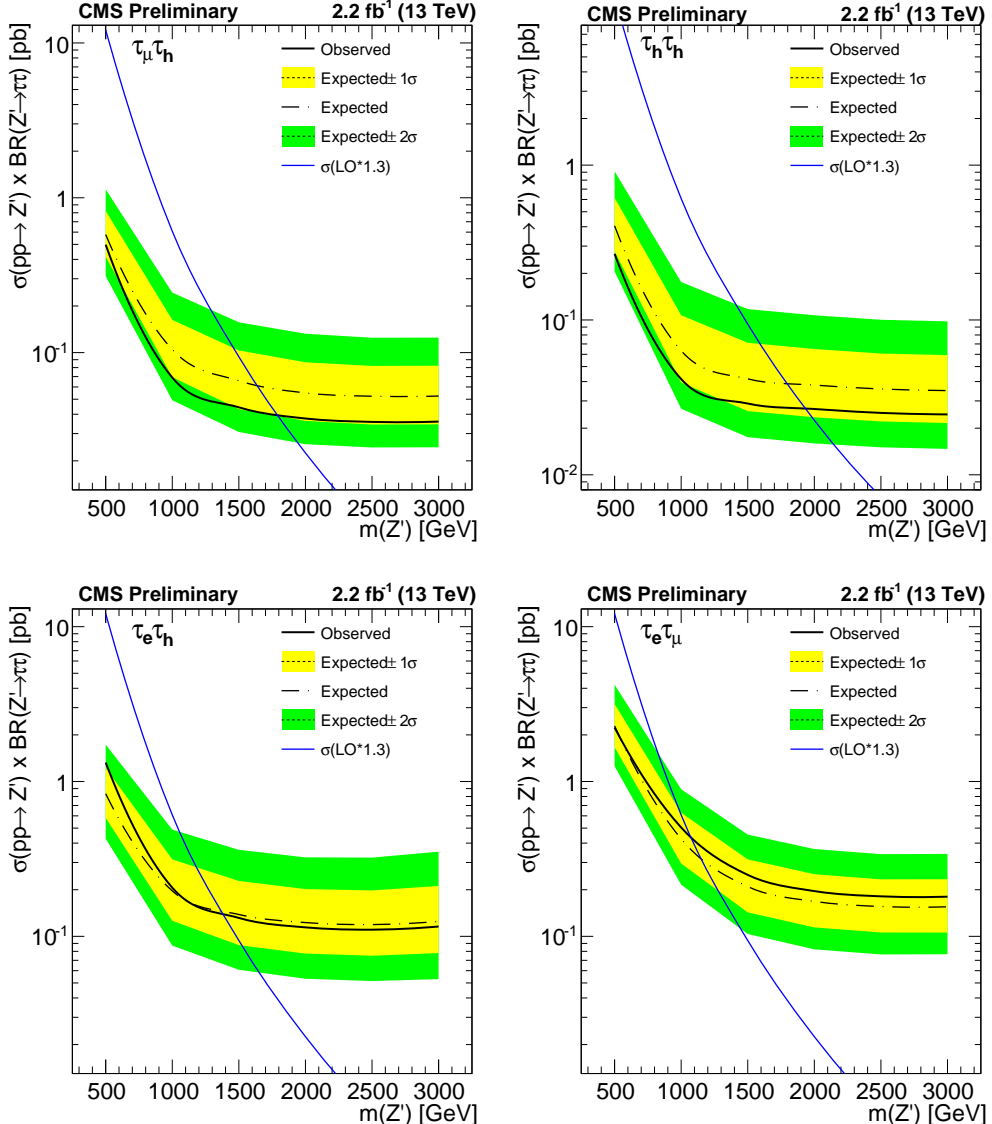


Figure 6.2: Expected and observed limits for the $\tau_\mu \tau_h$, $\tau_h \tau_h$, $\tau_e \tau_h$, $\tau_e \tau_\mu$ channels. A k factor of 1.3 has been used to scale the leading order (LO) signal cross-section.

the experimental value of $\sigma(pp \rightarrow Z') \times BR(Z' \rightarrow \tau\tau)$ exceeds the theoretical value. Below this point, we exclude the existence of Z' -like particles decaying to tau pairs. Figure 6.8 shows that we exclude the Z' below a mass of 1080 GeV/c².

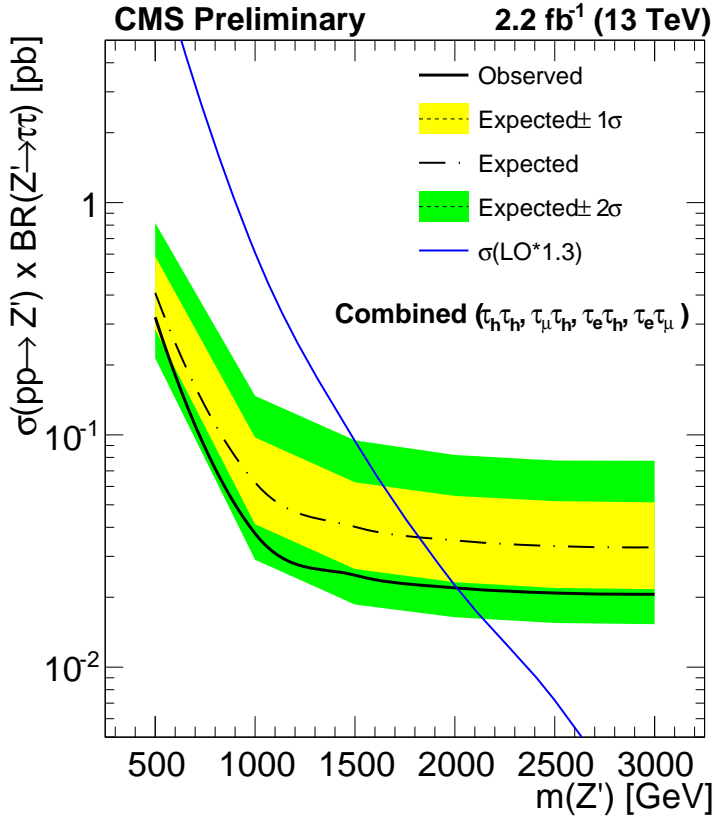


Figure 6.3: Combined expected limit for the $\tau_\mu\tau_h$, $\tau_h\tau_h$, $\tau_e\tau_h$, $\tau_e\tau_\mu$ channels.

Figure 6.4: Combined expected limit for the $\tau_\mu\tau_h$, $\tau_h\tau_h$, $\tau_e\tau_h$, $\tau_e\tau_\mu$ channels. A k factor of 1.3 has been used to scale the leading order (LO) signal cross-section.

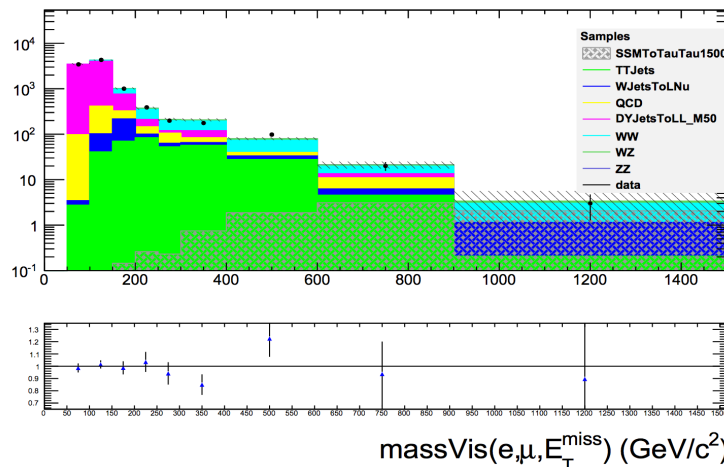


Figure 6.5: $m(e, \tau_h, \cancel{E}_T)$ distribution for SR in 8TeV search. A 1.5TeV Z'_{SSM} sample is also included.

$massVis(e, \mu, E_T) (GeV/c^2)$	[50,100]	[100,150]	[150,200]	[200,250]	[250,300]
Bkg expected in SR	3480±120	4230±120	1010±40	375±23	210±14
Data observed in SR	3430±60	4300±70	1000±30	388±20	198±14
$massVis(e, \mu, E_T) (GeV/c^2)$	[300,400]	[400,600]	[600,900]	[900,1500]	[0,1500]
Bkg expected in SR	207±13	80±5	21±4	3.3±2.3	9620±180
Data observed in SR	176±13	98±10	20±4	3.0±1.7	9600±100

Figure 6.6: Expected background rates compared to observed rates in bins of $m(e, \tau_h, E_T)$. Uncertainties are statistical in each bin.

$massVis(e, \mu, E_T) (GeV/c^2)$	[300,400]	[400,600]	[600,900]	[900,1500]	[0,1500]	> 400	> 900
$Z'_{SSM}(750)$							
Sig expected in SR	49±3	76±4	25.2±2.2	0.6±0.3	199±6	102±4	0.6±0.3
$s/\sqrt{s} + b$	3.188	5.914	3.827	0.305	2.006	6.983	0.305
$Z'_{SSM}(1000)$							
Sig expected in SR	10.3±0.7	22.6±1.1	19.2±1.0	1.58±0.28	62.3±1.8	43.5±1.5	1.66±0.29
$s/\sqrt{s} + b$	0.741	2.133	3.145	0.710	0.633	3.495	0.742
$Z'_{SSM}(1250)$							
Sig expected in SR	2.38±0.20	6.2±0.3	8.2±0.4	3.2±0.2	21.6±0.6	17.6±0.5	3.23±0.23
$s/\sqrt{s} + b$	0.174	0.633	1.592	1.251	0.220	1.549	1.260
$Z'_{SSM}(1500)$							
Sig expected in SR	0.75±0.07	1.87±0.11	3.09±0.14	2.06±0.11	8.44±0.22	7.07±0.20	2.10±0.11
$s/\sqrt{s} + b$	0.055	0.195	0.672	0.885	0.086	0.649	0.899
$Z'_{SSM}(1750)$							
Sig expected in SR	0.246±0.025	0.66±0.04	1.12±0.05	1.25±0.06	3.49±0.09	3.14±0.09	1.35±0.06
$s/\sqrt{s} + b$	0.018	0.070	0.256	0.582	0.036	0.293	0.623

Figure 6.7: Expected signal rates and associated significances in bins of $m(e, \tau_h, E_T)$.

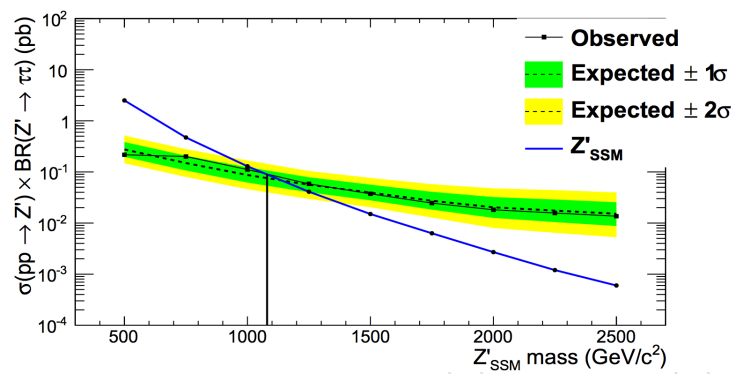


Figure 6.8: 95% CL upper limit on $\sigma(pp \rightarrow Z') \times BR(Z' \rightarrow \tau\tau)$ as a function of Z' mass. The color bands on the expected limits represent one standard deviation (green) and two standard deviations (yellow).